ISSN 1990-7931, Russian Journal of Physical Chemistry B, 2025, Vol. 19, No. 4, pp. 853–867. © Pleiades Publishing, Ltd., 2025.

ELECTRIC AND MAGNETIC PROPERTIES OF MATERIALS

# Synthesis of Phosphorus-Doped $MnCo_2S_4$ Nanosheet-Based Porous Spheres for Hybrid Supercapacitors

**Z. Sheibanizadeh[a], Z. Khalaj[a, *, **], K. Behzad[a], M. Z. Pedram[b], and M. Monajjemi[c]**

[a] *Department of Physics, Shahr-e-Qods Branch, Islamic Azad University, Tehran, Iran*

[b] *Faculty of Mechanical Engineering- Energy Division, KN Toosi University, Tehran, Iran*

[c] *Department of Chemical Engineering, Central Tehran Branch, Islamic Azad University, Tehran, Iran*

**e-mail: khalaj.z@gmail.com*

***e-mail: z.khalaj@qodsiau.ac.ir*

Received December 30, 2024; revised April 11, 2025; accepted April 21, 2025

**Abstract**—Phosphorus-doped $MnCo_2S_4$ hollow spheres with a heterogeneous, nanosheet-assembled architecture were synthesized via a simple gas–liquid diffusion method under ambient conditions, in contrast to conventional hydrothermal and gas-phase phosphating techniques. Ammonia diffusion into a homogeneous manganese–cobalt sulfate solution led to the formation of well-dispersed hollow spheres with lamellar structures, promoting efficient electron transport and enhanced electrochemical activity. Phosphorus atoms partially substituted sulfur in the lattice, generating abundant vacancies that improved conductivity and charge transfer kinetics. The resulting electrode exhibited a high specific capacity of 928.2 C $g^{-1}$ at 1 A $g^{-1}$ and excellent cycling stability, retaining 93.8% of its capacity after 10 000 cycles. A hybrid supercapacitor was assembled using the phosphorus-doped $MnCo_2S_4$ as the cathode and activated carbon as the anode in 6 M KOH electrolyte. The device delivered a specific capacity of 225.6 C $g^{-1}$ at 1 A $g^{-1}$, retained 75.5% capacity at 30 A $g^{-1}$, and achieved a high energy density of 55.8 Wh $kg^{-1}$ with a power density up to 24453.6 W $kg^{-1}$, demonstrating excellent rate performance and long-term stability.

**Keywords:** transition-metal sulfides, phosphorus-doped, nanosheet assembly, hybrid supercapacitor

**DOI:** 10.1134/S1990793125700678

## INTRODUCTION

Growing concern about environmental issues and the rapid use of fossil fuels drives the development of efficient, clean energy storage devices [1, 2]. Presently, most primary energy consumption is derived from nonrenewable fossil fuels (e.g., gas, coal, and oil), which contributes to a rise in pollution and, ultimately, a deterioration in health. Energy storage devices, for instance supercapacitors and batteries, are essential for effectively utilizing inexpensive renewable and clean energy sources [3–5]. The supercapacitor has the advantage of providing long cycle life (350000 cycles), high power density, and being low-cost and environmentally friendly [6, 7]. Although the supercapacitor has a high-power density, it still requires a higher energy density and stability level to become a practical power source [8–11]. To increase their energy density, hybrid supercapacitors (HSCs) provide a perfect solution. These hybrid supercapacitors are distinguished in the energy storage field due to their unique features, combining the energy density of faradaic electrodes with the long lifetime and high-power density of non-faradaic electrodes in a device [12–16].

Specifically, a battery type electrode can facilitate a higher capacity via a fast-reversible redox reaction [17–21]. By contrast, an electrode with a pseudocapacitive or capacitive structure could provide a wider voltage window and a higher power output. Hence, high-efficiency energy storage depends heavily not only on the configuration engineering of the device but also on the ingredients and rational structures of its electrode materials. Several hybrid supercapacitors have been constructed using transition metal-based materials as positive electrodes, including hydroxides, oxides, sulfides, etc. [16, 22, 23].

Diverse metals have been used to purify water and air, as well as to produce nanosensors, gas sensors, and energy storage devices [24–26]. Various transition metals particularly transition metal sulfides (TMSs), have emerged as promising battery-type electrodes for hybrid supercapacitors (owing to their multiple valence states, reversible faradaic redox activity, tunable composition, and substantial theoretical capacitance/capacity Transition metal sulfides have gained considerable attention as alternative battery-type electrodes for HSCs due to their numerous valence states, availability of faradaic redox reactions, adjustable composition, and substantial theoretical capacitance/capacity) [27–30]. The above achievements have inspired extensive efforts to synthesize and design

hybrid metal sulfides that serve as electrodes for supercapacitors. Several hollow structures binary hybrid metal sulfides have been investigated for electrode materials in supercapacitors, including Zn–Ni sulfides, Ni–Mn sulfides, Co–Ni sulfides, and Cu–Ni sulfides [31–34]. Liu et al. have recently synthesized a hierarchical heterostructured $Co_9S_8$–$NiCo_2S_4$ core-shell nanoneedle electrode material that delivers at 1 A $g^{-1}$ specific capacitance of 337.78 mA h $g^{-1}$. According to Wang et al, a three-dimensional (3D) hybrid nickel-cobalt sulfide was synthesized wrapped in a thin carbon layer with a high area capacity of 856.6 C $g^{-1}$ at a current density of 1 A $g^{-1}$ [35, 36].

Nevertheless, the low intrinsic conductivity of TMSs and their propensity to restack indefinitely result in slow charge/ion transfer and insufficient electroactive sites, contributing considerably to their poor electrochemical characteristics [37–39]. As a result, a variety of strategies have been developed to solve the problems discussed above, including elemental doping, defect engineering, hybrids with conductive materials, etc. [40–42]. For this reason, many proposals have been made regarding various metallic, nonmetallic, metalloid and nanomaterials as semiconductors through doping for the design of energy storage devices [43–45]. In this regard, dual-ligand modification approaches are essential to improve the electrochemical characteristics of electrode materials [46, 47]. By benefitting from the synergistic effect in M–S/X and regulating ion-covalent properties, the specific electronic structure, improved chemical activity, and greater conductivity could be achieved to promote redox reactions. Hence, a more feasible and simple method of fabricating sulfide electrodes with porous features and dual-ligands has proven highly popular in controlling their electronic structure, providing significant energy storage capability, and introducing dual-reactive sites [46, 48].

By recombining different transition metal sulfides, heterogeneous structures can be formed, optimizing electron/migration paths, leading to significantly enhanced electrochemical energy storage and providing access to all surface active sites [49, 50]. In particular, because of the perfect synergy between Mn and Co, nickel-cobalt sulfide has a higher capacitance than other binary metal sulfides [51, 52]. A recent study reported the development of $MnS_2$–$CoS_2$ nanosheets with rich lattice interfaces and widespread nanopores by Wu et al. This unique structure impressively enhances the ion diffusion rate and shortens the electron transport path. Moreover, the synergistic effect between the bimetals contributes to the electrochemical performance, resulting in a high specific capacitance of 1158 F $g^{-1}$ at 1 A $g^{-1}$ [53, 54]. Guan et al. developed structurally controllable nanostructures of $MnCo_2S_4$, characterized by large specific surface areas (SSA) and a layered structure. With this unique structure, $MnCo_2S_4$ has a specific capacitance of 938 F $g^{-1}$ at 20 A $g^{-1}$ and a retention rate of 95% at 10 A $g^{-1}$ [55].

Generally, morphology and nanostructure have a considerable influence on electrochemical performance. Developing electrode materials with the effective morphology and nanostructure is one of the most promising ways of increasing electrochemical efficiency [56–59]. Many studies have shown that 3D hollow structures are highly stable due to their ability to buffer volume expansion, prevent structural distortion, accommodate mechanical strain, and enhance cycling performance. Moreover, a hollow interior may also be considered an ion buffering container, which can ensure ion supply and reduce ion transport paths during redox reactions. For these reasons, ligands have been used as a template for preparing hollow sphere structures. Moreover, structural engineering has emphasized the importance of enhancing the internal structure of materials in order to take advantage of the great advantage of hollow sphere structures. Several modified hollow sphere structures have been fabricated, including multi-shell layered structures, single/double yolk shell layered structures, and urchin-like structures [59–61].

Nevertheless, electrochemical performance heavily depends on electrode-electrolyte contact area and the number of exposed active sites, both of which can be improved by increasing the SSA of the electrode. Therefore, the specific area is the most important aspect of improving the electrochemical performance. In light of this, substantial research has investigated various methods for preparing complex hollow architectures [62–64]. A self-templating approach is one of the more relevant strategies for complex hollow architectures, considering their large-scale synthesis, cost-effectiveness, and ease of synthesis [65]. Currently, the hydrothermal method is generally used for the morphology control of nanostructures, in which the ligands play a vital role.

It is still possible to enhance the stability of metal sulfide electrodes as well as increase their capacity, which is a significant challenge for a wide range of supercapacitors [66]. Generally, a well-tuned nanostructure can support more reaction sites, reduce ion diffusion paths, and decrease electrochemical strain [23, 67]. In order to achieve high energy density, heteroatom doping is an effective method for optimizing the internal electronic structure of materials [68]. There is a lone pair of electrons on the 3*p* and 3*d* orbitals of a P atom, which enables it to absorb electrons from metal atoms. Therefore, the P dopant is capable of advantageously controlling both surface charge states and local charge density, thereby enhancing the electrochemical performance of the doped sample. Liu et al. reported a phosphorus-doped $Co_3O_4$ composite, exhibiting a high specific capacitance of 984 F $g^{-1}$ (1 mA $cm^{-2}$) and ultrahigh cycle life [69]. Chu successfully prepared P-doped $NiCo_2O_4$ nanowires on nickel

foam substrates. It demonstrated outstanding specific capacitance of 2747.8 F $g^{-1}$ (1 A $g^{-1}$) and remarkable rate capability. $NiCo_2O_4$ electrodes doped with P are significantly more conductive due to the abundance of oxygen vacancies and the introduction of the P element [70].

According to Wen and colleagues, P-doped $CoS_2$ is an extremely stable and active electrocatalyst for hydrogen evolution. Due to this, it is anticipated that adding sulfur to CoP will enhance cycling stability and, therefore, the overall performance of the supercapacitor [71].

Based on the above considerations, we have designed a novel process to promote metal sulfide stability via thermal phosphodation. In the first step, the $MnCo_2S_4$ hollow spheres (MCSHSs) were synthesized by a two-step gas-liquid diffusion method, followed by a sulfurization treatment. Then, through this phosphorization process, the heteroatom P was doped into MCSHSs by thermal decomposition of $NaH_2PO_2$. By developing this electrode material, we intend to: (i) create porous hollow sphere structures that promote fast ion diffusion, (ii) enhance electrochemical performance by providing hollow sphere structures with high SSA, and (iii) further enhance overall electrode conductivity. By using PH3 gas in the phosphating process, heterogeneous MCSHS structures were efficiently introduced with P atoms. In particular, the three-electrode cell containing the nanosheet-assembled heterogeneous phosphorus-doped $MnCo_2S_4$ hollow spheres (P–MCS-HSs ) electrode showed a capacitive improvement by sulfidization. Ultimately, a P–MCS-HSs electrode was used to test an assembled SC device.

## EXPERIMENTAL

### *Preparation of Primary Material*

In beaker A, a solution of $CoSO_4{\cdot}7H_2O$ (3.0 mmol) and $MnSO_4{\cdot}6H_2O$ (1.5 mmol) was prepared by dissolving them in 50 mL of deionized water to obtain a red solution. Approximately 15 mL of concentrated ammonia (25%) was added to 50 mL deionized water in beaker B, which was then transferred to the above 20 L sealed container and left for several minutes until precipitation was observed [72]. After the precipitation had been collected, it was washed in absolute ethanol and DI water, respectively, and dried overnight in a vacuum oven at 80°C. Then, the precipitation was under heat treatment at the rate of 2°C/ min at 350°C to yield the MCOSs.

### *Preparation of $MnCo_2S_4$ Hollow Spheres*

In a tube furnace, MCO powder was placed in a ceramic boat. The sulfur powder was placed in another ceramic boat at the upstream side of the furnace. The sample was then heated to 350°C under $N_2$ gas at 5°C/min. Following the cooling process in the furnace, samples of MCSHSs were collected.

### *Preparation of Phosphorus-Doped $MnCo_2S_4$ Hollow Spheres*

In the quartz boat, 175 mg of $NaH_2PO_2$ were placed near the gas inlet. A sample of 10 mg of MCSHSs was placed on the opposite side of the quartz boat. $NaH_2PO_2$ and MCS were heated to 300°C in $N_2$ atmosphere at a rate of 2°C/10 min. As a result of cooling to room temperature, P–MCS-HSs electrode material was obtained.

### *Characterizations*

X-ray diffraction was used to examine the composition and phase structure of the prepared samples (XRD, PW3040/60) using Cu Kα radiation ($\lambda \approx$ 1.54178 A). By using field emission scanning electron microscopy (FE-SEM, TESCAN; Mira III LMU; Czech Republic) and transmission electron microscopy (TEM; Philips CM200 instrument) with an accelerating voltage of 200 kV, the morphology and microstructures of the as-prepared products were investigated. In addition, energy dispersive spectrometry (EDS) was employed to determine the distribution of elements in the prepared sample. X-ray photoelectron spectroscopy (XPS; Thermo Scientific; ESCALAB 250Xi Mg X-ray source) determines the elemental composition and superficial electronic states of electrode materials (Thermo Scientific, ESCALAB 250Xi Mg X-ray source). According to the BET (Brunauer–Emmett–Teller) and BJH (Barrett–Joyner–Halenda) models, the textural features of the as-prepared materials were estimated (Micromeritics ASAP 2010).

### *Electrochemical Tests*

The three-electrode configuration used Pt foil as the counter electrode, 6 M KOH as the electrolyte, and Ag/AgCl as the reference electrode. An electrode was prepared by mixing acetylene black, polyvinylidene fluoride with methyl 2-pyrrolidone, and as prepared material in a mortar in the optimal mass ratio of 1 : 1 : 8. As a next step, The prepared paste was uniformly applied to nickel foam (1 by 1 cm), which was then dried for 15 h at 70°C. In the following steps, a hydraulic press was used to apply a pressure of 10 MP. The active substance loading was approximately 4.0 mg $cm^{-2}$. Anode (AC) fabrication was carried out according to a similar procedure. The EIS, GCD, and CV profiles were acquired at room temperature using a PGSTAT 204 (Echo Chemie, Netherlands). Based on the GCD plot, the specific capacity values of electrodes were determined as follows [73]:

$$C_s\,(\mathrm{C/g}) = \frac{2I\int V dt}{m\,V}. \quad (1)$$

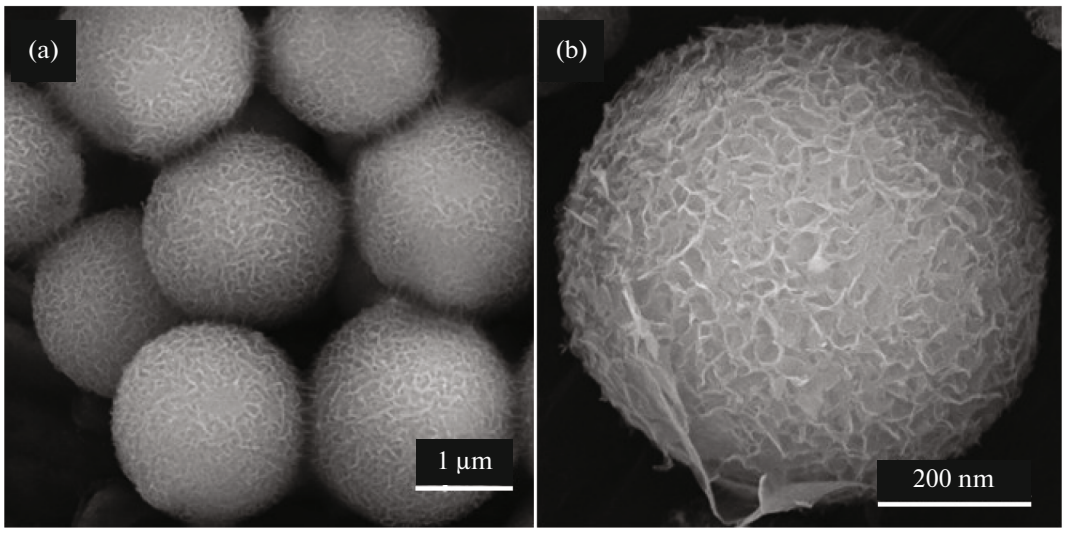


**Fig. 1.** (a, b) FESEM image of the MCOSs.

Using the formula (1), $C_s$ displays the specific capacitance (C $g^{-1}$), m indicates the mass of the active electrode (g), *dt* signifies the discharge duration (s), *V* indicates the voltage window (V), and *I* signifies the discharge current (A).

Moreover, the Coulombic Efficiency (CE) of the P–MCS-HSs and hybrid supercapacitor was determined utilizing the formula (2) [74]:

$$\mathrm{CE} = \frac{t_d}{t_c}. \quad (2)$$

In formula (2), $t_c$ and $t_d$ indicate the times of charge and discharge, respectively.

### *Designing of Apparatus*

An aqueous hybrid supercapacitor apparatus (P–MCS-HSs/NF(+)‖AC/NF)(–)) was constructed to investigate the potential application of the P–MCS-HSs electrode. An apparatus was constructed using nickel foam (NF) coated with P–MCS-HSs cathode electrode and AC anode electrode, a cellulose paper separates the two electrodes in order to minimize short circuits. To obtain maximum electrochemical performance, electrodes were soaked in KOH before construction to achieve highest electrochemical performance. Finally, a hot sealer sealed the electrodes and cellulose paper in a non-conductive bag. A proper balance will be required before constructing the fabricated apparatus to ensure high efficiency. The mass ratio of optimized P–MCS-HS to AC was calculated according to the charge balance principle (Q+ = Q–) following the calculation formula (3) [73]:

$$\frac{m_+}{m_-} = \frac{C_- \Delta V_-}{C_{s+}}, \quad (3)$$

where $\Delta V$ (V), $m$ (g), $C$ (F $g^{-1}$), and $C_s$ (C $g^{-1}$) indicate the voltage window, the mass of electrode materials, specific capacitance, and specific capacity, respectively. It should note that + denotes cathode material, whereas—denotes anode material. Using Eq. (3), it can be determined that the mass ratio between P–MCS-HS and AC is 1 : 5.7. Similarly, the mass loadings of P–MCS-HS and AC are 4 and 23.25 mg, respectively. As a result of formulas (4) and (5), the energy density ($E$, W h $kg^{-1}$) and power density ($P$, W $kg^{-1}$) of as-made P–MCS-HSs /NF(+)‖AC/NF)(–) were calculated [75]:

$$E\,(\mathrm{W\,h/kg}) = \frac{I\int V dt}{3.6M}, \quad (4)$$

$$P\,(\mathrm{W/kg}) = \frac{E}{\Delta t} \times 3600. \quad (5)$$

## RESULTS AND DISCUSSION

### *Characterization*

We first synthesized $MnCo_2S_4$ hollow spheres (MCSHSs) by the three-stage gas-liquid diffusion method at room pressure and temperature, followed by a sulfurization treatment. Then, through this phosphorization process, the heteroatom P was doped into MCSHSs by thermal decomposition of $NaH_2PO_2$. Due to the heterogeneous nanosheet-assembly structure of P–MCS-HSs, ions are able to migrate effectively to the deep regions of the electrodes. As a result, the P–MCS-HSs electrode exhibits significant capacity storage and performance. To determine the morphology of the electrode materials, FE-SEM and TEM images were collected of the as-fabricated products, as shown in Figs. 1 and 2. According to Fig. 1, the MCOSs product exhibits a hollow sphere morphology

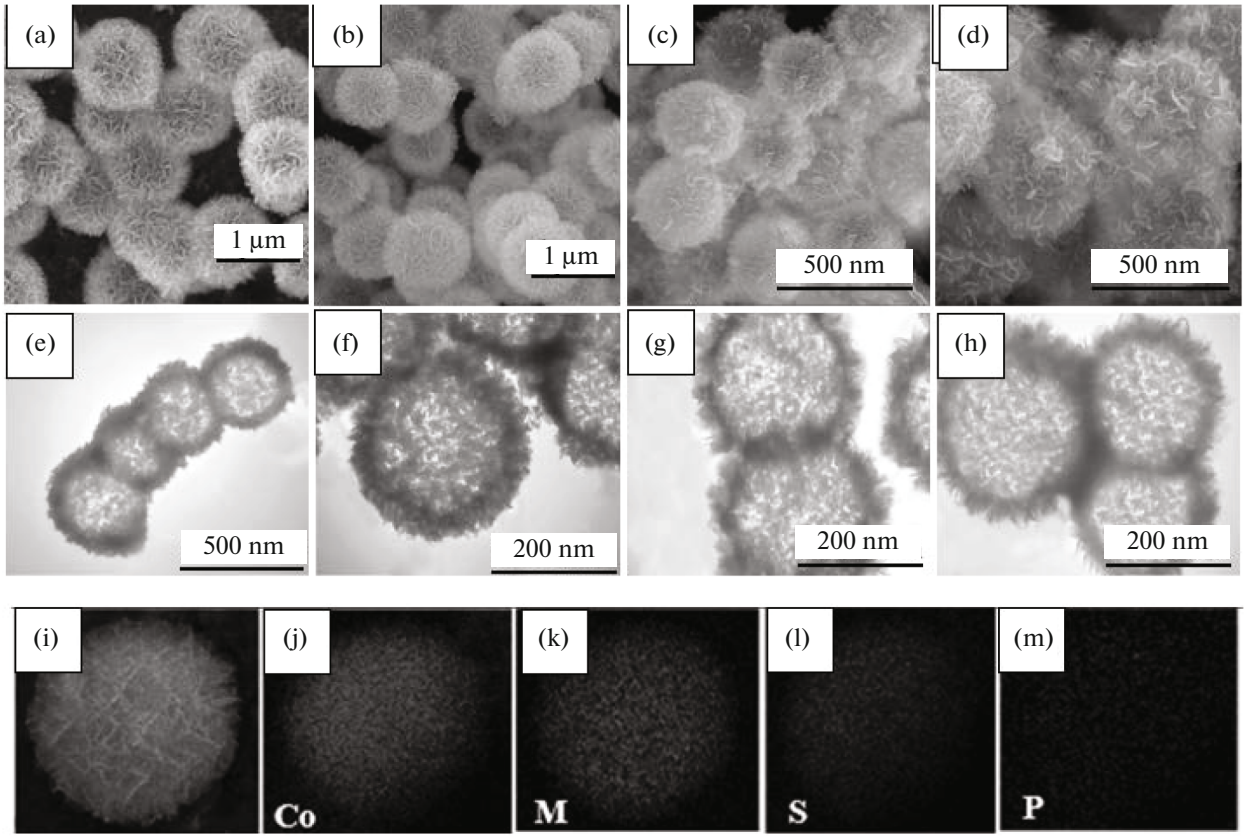


**Fig. 2.** (a, b) FE-SEM images of the MCSHSs. (c, d) FE-SEM images of the P–MCS-HSs. (e, f) TEM images of the MCSHSs. (g, h) TEM images of the P–MCS-HSs. (i–m) EDX mapping of the P–MCS-HSs.

comprised of self-assembled nanosheets with relatively rough surfaces. Following the sulfurization treatment, MCOSs were converted into MCSHSs, and the morphologies of the as-prepared MCSHSs samples are shown in Figs. 2a, 2b. As shown in the FE-SEM images, MCSHSs exhibit a spherical-like morphology and a hollow sphere structure composed of nanosheets that are achieved through MCOSs sulfidation. According to the corresponding TEM images (Figs. 2e, 2f), the surface of each nanosphere was covered by numerous ultrathin and disordered nanosheets, which displayed highly porous properties as well as hierarchical and open structures. This results in a greater contact area for the active material and a faster ion transfer path, increasing electrochemical performance. Figures 2c, 2d displays the FE-SEM images of the P–MCS-HS sample. The FE-SEM image indicates that P–MCS-HSs inherit the spherical morphology of the MCSHSs structure. P–MCS-HSs morphology appears collapsed, which may be caused by gradual cracks in the sheet structure during phosphorization. As a result, the shape of this MCSHS might be favorable to the penetration of $PH_3$ and the reaction between MCSHS and $PH_3$ during the phosphorization process. In addition, the P–MCS-HSs nanostructure obtained by phosphorization treatment preserves the hollow sphere structure. There are many intertwined small nanosheets on the surface, which may result from phosphide formation. However, the nanosheets of P–MCS become considerably thicker than the MCSHSs structure.

Moreover, a hollow sphere doped with phosphorus also has a more compact structure, which in turn accelerates ion diffusion, has a greater surface area for charge transfer, and exposes more sites for electrical activity. Meanwhile, the growth of P–MCS-HSs exhibits remarkable integrity and uniformity. The heterostructure provides an optimal pathway for electron migration and further exposes active reaction sites. TEM was used to further investigate the inherent properties of the products as made. P–MCS-HSs sample images (Figs. 2g, 2h) showed hollow nanospheres with a highly porous texture, suggesting the sheet structure may have cracked slowly during phosphorization. With such unique structural features, a large number of active sites could be provided, and electrolytes could be effectively absorbed, thereby enhancing the super capacitive properties of the P–MCS-HSs sample. The elemental distribution in P–MCS-HSs was analyzed through elemental mapping, as depicted in Figs. 2i–2m. The observed results indicate that the Co, Mn, S, and P elements are uniformly distributed entirely the area, inferring the efficient formation of P–MCS-HSs structures.

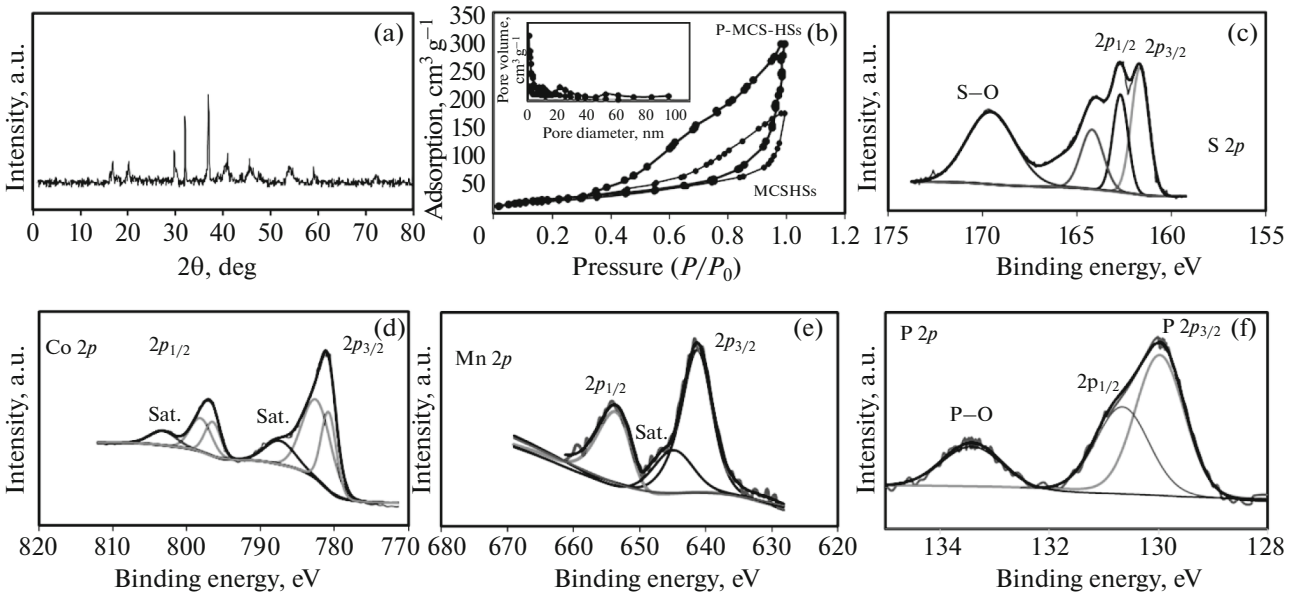


**Fig. 3.** (a) XRD pattern of the P–MCS-HSs. (b) BET and BJH of the P–MCS-HSs and MCSHS. (c) S 2*p* XPS spectra of the P–MCS-HSs. (d) Co 2*p* XPS spectra of the P–MCS-HSs. (e) Mn 2*p* XPS spectra of the P–MCS-HSs. (f) P 2*p* XPS spectra of the P–MCS-HSs.

The phase structure of the P–MCS-HSs sample was determined by X-ray diffraction (XRD) in Fig. 3a Diffraction peaks are well indexed to spinel $MnCo_2S_4$ and MnCoP in the XRD pattern. These samples present major diffraction peaks at 16.3°, 27.2°, 31°, 31.5°, and 36.5°, corresponding to planes (111), (220), (311), (222), and (400) (JCPDS no. 73–1703) [76]. As well, the diffraction peaks 43.2°, 47.3°, 56.9°, 31.5°, and 59.2° correspond to the standard peaks of MnCoP (JCPDS no. 042-0932) [8, 77]. To investigate the porosity and surface area of P–MCS-HS and MCSHS samples, BJH and BET analyses were conducted. Based on the adsorption–desorption graphs of both materials, type IV isotherms with obvious hysteresis loops were observed, confirming their mesoporous nature. Consequently, the P–MCS-HSs sample possessed a specific surface area of 224.6 $m^2\ g^{-1}$, higher than the MCSHS sample (SSA of 134.2 $m^2\ g^{-1}$). The BJH test was used to estimate the features of the pore size distributions of both samples (inset of Fig. 3b) [78]. Supercapacitors with their mesoporous properties and such a large SSA can boost ion-electron trans-

**Table 1.** Comparison between the supercapacitor made in this work and other supercapacitors

| Material | Three-electrode system | | Rate capability | Energy density, W h $kg^{-1}$ | Power density, W $kg^{-1}$ | References |
|---|---|---|---|---|---|---|
| | specific capacitance/C $g^{-1}$ | cycle retention | | | | |
| NiCoP | 697.3 at 1 A $g^{-1}$ | 50000, 90.2% | 91.1% at 20 A $g^{-1}$ | 35.6 | 838.7 | [100] |
| NiCoMn-S | 661 at 1 A $g^{-1}$ | 1000, 86.4% | 66.56% at 50 A $g^{-1}$ | 42.1 | 750 | [28] |
| Mn-CoP/NF | 455.7 at 0.5 A $g^{-1}$ | 20000, 89% | 77.4% at 10 A $g^{-1}$ | 14.82 | 312 | [101] |
| $Ni_2P$/Ni/C | 257.1 at 1 A $g^{-1}$ | 5000, 84.3% | 60.5% at 10 A $g^{-1}$ | 25.4 | 750 | [102] |
| Ni–Co–P/$PO_x$/C | 635.7 at 1 A $g^{-1}$ | 5000, 77.3% | 62.7% at 30 A $g^{-1}$ | 37.59 | 800 | [103] |
| Ni–Mn–S@$NiCo_2S_4$ | 939, at 1 A $g^{-1}$ | 5000, 90.3% | 69.2% at 20 A $g^{-1}$ | 59.1 | 344.8 | [104] |
| Ni–Co phosphide | 650.5 at 1 A $g^{-1}$ | 1000, 85% | 51% at 1 A $g^{-1}$ | 49.4 | 11.7 | [105] |
| $Ni_2P/Co_3O_4$/NCQDs | 828 at 1 A $g^{-1}$ | 6000, 90.5% | 83.9% at 20 A $g^{-1}$ | 53.5 | 772.9 | [106] |
| P–MCS-HSs | 928.2 at 1 A $g^{-1}$ | 10000, 93.8% | 70.4% at 30 A $g^{-1}$ | 55.8 | 810.3 | This work |

port kinetics, increase their energy and power densities, and enhance their longevity [52].

This XPS analysis was conducted to determine in more detail the surface species and chemical states of the P–MCS-HSs, as illustrated in Figs. 3c–3f. The S 2*p* characteristic peak of P–MCS-HSs is fitted to two peaks at 163.6 and 164.9 eV, which correspond to S $2p_{3/2}$ and S $2p_{1/2}$, respectively (Fig. 3c) [77]. The characteristic peak at 169.0 eV is due to $SO_4^{2-}$ species, which manifests in the slight oxidation of the P–MCS-HSs surface. Figure 3d shows the Co 2*p* XPS spectrum of P–MCS-HSs. There are characteristic peaks at 782.9 and 781.6 eV, corresponding to Co $2p_{3/2}$ of the $Co^{2+}$ and $Co^{3+}$ species, respectively. Following the literature, two oxidation states are observed, $Co^{3+}$ and $Co^{2+}$ [79]. According to Fig. 3e the Mn 2*p* spectrum displays two Mn $2p_{1/2}$ and Mn $2p_{3/2}$ peaks, which may be deconvoluted into fitting peaks for $Mn^{2+}$ (centered at 641.1 and 652.7 eV) and $Mn^{3+}$ (centered at 643.1 and 655.2 eV) [80, 81]. The P 2*p* spectrum (Fig. 3f) reveals that the two peaks at 129.4 and 129.9 eV correspond to P 2*p*3/2 and P 2*p*1/2, respectively, confirming the successful formation of the M–P bond (M = Mn and Co) [82, 83]. Further characteristic peak at 135.2 eV is attributed to the P–O bond of P–MCS-HSs, which results from the surface oxidation of Mn- and Co–P exposed to air. As a result of exposure to air, Mn– and Co–P surfaces oxidize, resulting in the characteristic peak at 135.2 eV [8, 83].

### *Electrochemical Tests*

Firstly, we analyze electrode performance as a supercapacitor in the three-electrode cell to determine the suitability of the as-produced materials for use in hybrid supercapacitors. Moreover, the specific conductivity of KOH has been demonstrated to be higher at a 6 M concentration than at lower concentrations which is more suitable for enhancing the performance of supercapacitors [84, 85]. As shown in Fig. 4a, the CVs were measured at 50 mV/s for MCOSs, MCSHSs, and P–MCS-HSs electrodes in an operating voltage window (0–0.60) V vs. Ag/AgCl. As can be seen from the CV plots, the area integrated is arranged in the following order: P–MCS-HSs > MCSHSs > MCOSs. Figure 4B illustrates a similar result for P–MCS-HSs, which has a longer discharge time than MCSHSs and MCOSs, suggesting a better supercapacitor performance. As shown in Figs. 4a, 4b, the CV (50 mV $s^{-1}$) and GCD (1 A $g^{-1}$) comparison curves for samples are shown. The P–MCS-HSs electrode displays a larger CV area and a longer discharge time in the GCD plot, indicating a higher capacity. Figure 4C illustrates the comparison of the capacity values of these electrodes at 1 A $g^{-1}$. P–MCS-HSs electrode delivered the highest capacity of these electrodes with 928.2 C $g^{-1}$, compared with 874 C $g^{-1}$ for MCSHSs, and 415 C $g^{-1}$ for MCOSs at 1 A $g^{-1}$ (Fig. 4c).

As-made electrode CV profiles exhibit noticeable peaks corresponding to reduction and oxidation, suggesting battery-type faradaic behavior resulting from electron exchange during redox reactions [86, 87]. Following equations can be used to explain redox reactions related to P–MCS-HSs electrode ]8, 76, 88, 89].

$$MnCoS_4 + OH^- + H_2O \leftrightarrow MnSOH + 2CoSOH + e^-, \quad (6)$$

$$CoSOH + OH^- \leftrightarrow CoSO + H_2O + e^-, \quad (7)$$

$$CoP_x(OH) + OH^- \leftrightarrow CoP_xO + H_2O + e^-, \quad (8)$$

$$MnCoP + 2OH^- \leftrightarrow MnP_{(1-x)}(OH) + CoP_x(OH) + 2e^-, \quad (9)$$

$$CoP_x(OH) + OH^- \leftrightarrow CoP_xO + H_2O + e^-. \quad (10)$$

Meanwhile, the peak current and electroactive area of the CV plot for the P–MCS-HSs electrode are more significant than those of other electrodes, which confirms the high capacity of the electrode after P doping by thermal decomposition of $NaH_2PO_2$. The P–MCS-HSs demonstrate higher capacity performance because of their unique properties, such as highly porous networks, excellent SSA, and high conductivity [90]. As a result of the doping of heteroatom P in the electrode, the defect degree is increased, in turn enhancing the reaction sites and faster pseudocapacitance activity of the electrode [91, 92]. Incorporating P atoms into MCSHS crystalline structure can regulate electrode material properties, create more active sites where electrolyte ions can contact each other, and relieve the strain on the P–MCS-HSs electrode during long cycles by ensuring superior structural stability and fast electron transfer [93].

The EIS test was also performed to determine the origin of the excellent super capacitive performance of P–MCS-HSs and MCSHS. As shown in Fig. 4d, the Nyquist plots are displayed for P–MCS-HSs and MCSHS electrodes. Z-view software was used to fit the EIS data. Further, the equivalent circuit model is displayed in Fig. 4d (inset). The charge transfer resistance $R_{ct}$ is related to the semicircle examined in the high-frequency zone in the equivalent circuit. The intersection of the high-frequency zone with the horizontal axis indicates the $R_s$ (internal resistance), which depends upon the intrinsic resistance of the substrate, the ionic resistance of the electrolyte, and the contact resistance of the electrode interface and NF current collector. It is worth noting that the element $R_w$ possesses Warburg resistance, which facilitates ion diffusion during the electrochemical reaction. The P–MCS-HSs electrode showed a vertical line with a higher slope, indicating a fast charge transfer kinetics and lower diffusion resistance than other electrodes

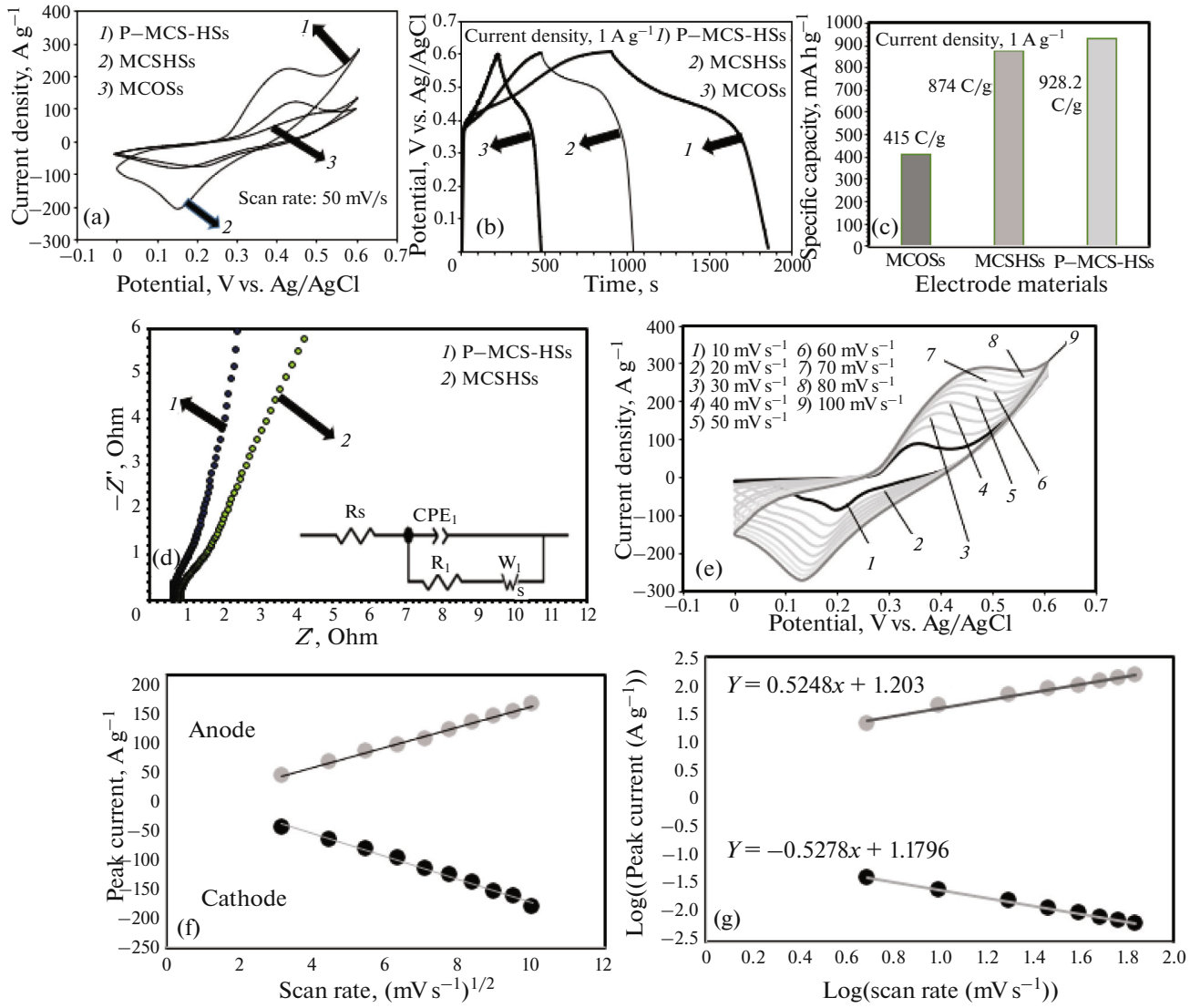


**Fig. 4.** (a) CV curves of the MCOSs, MCSHS, and P–MCS-HSs electrodes at 50 mV $s^{-1}$. (b) GCD plots of the MCOSs, MCSHS, and P–MCS-HSs electrodes at 1 A $g^{-1}$. (c) Specific capacities of MCOSs, MCSHS, and P–MCS-HSs electrodes at 1 A $g^{-1}$. (d) Nyquist plots of the MCSHS and P–MCS-HSs electrodes (inset reveals the equivalent circuit model). (e) CV plots of the P–MCS-HSs electrode from 10 to 100 mV $s^{-1}$. (f) The linear plot of anodic and cathodic peak currents as a function of the square root of the sweep rate. (g) The linear curve of the logarithm of peak current as a function of the logarithm of the sweep rate.

[94]. The P–MCS-HSs electrode presents ultra-low $R_{ct}$ and $R_s$ values of 0.23 and 0.62 Ohm, respectively, which are considerably smaller than that of MCSHS ($R_{ct}$ = 0.68 Ohm; $R_s$ = 0.92 Ohm). P–MCS-HSs electrode have low $R_{ct}$ and $R_s$ values, suggesting a higher electrical conductivity and faster reaction kinetics. In addition, CV profiles of P–MCS-HSs electrode were analyzed in detail by varying sweep speeds from 10 to 100 mV $s^{-1}$, as shown in Fig. 4e. As the P–MCS-HSs electrode shows detectable redox peaks from the beginning, these peaks show no signs of disappearing even at high sweep speeds, corroborating its effective reversibility.

In addition, by increasing the sweep speed from 10 to 100 mV $s^{-1}$, it has been observed that both the cathodic and anodic peaks shift toward lower potentials, which can be attributed to the polarization of P–MCS-HSs electrode. From the CV plots, the reaction kinetics of the MCS-HSs electrode are further investigated. According to the power law ($I = a\upsilon^b$), two distinct charge storage mechanisms are responsible for the total charge storage of the CV profile, the capacitive-type and diffusion-type mechanisms. These two mechanisms are described by the sweep speed ($\upsilon$) and peak current density ($i$) correlation [49]. A $b$ value close to 1.0 indicates that a capacitive storage process contributes to the electrochemical reaction,

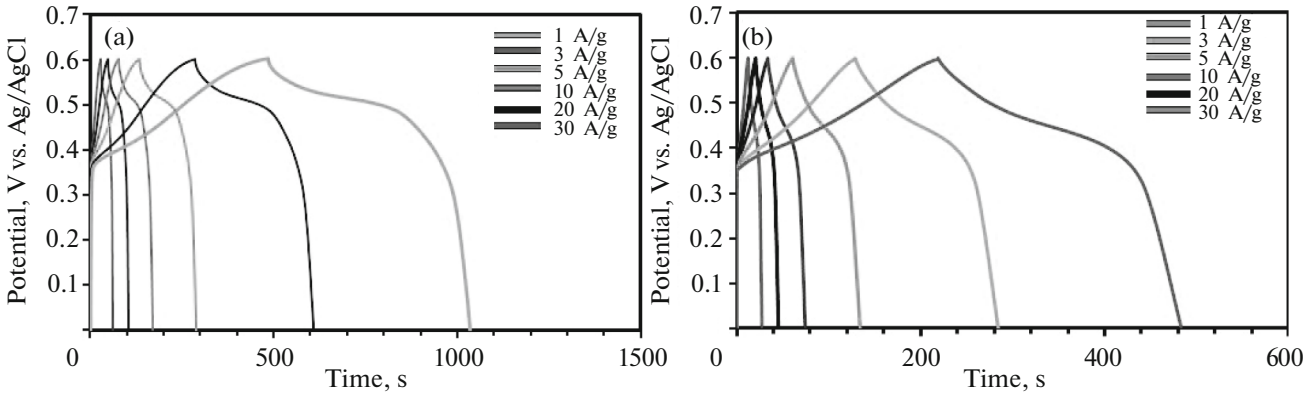


**Fig. 5.** (a) GCD plots of the P–MCS-HSs electrode from 1 to 30 A $g^{-1}$. (b) Specific capacities vs. current densities of the MCOSs, MCSHS, and P–MCS-HSs electrodes. (c) Longevity and Coulombic efficiency of the P–MCS-HSs electrode at 15 A $g^{-1}$. (d) Capacitive contributions and diffusion-controlled contributions of P–MCS-HSs electrode at various scan rates from 10 to 100 mV $s^{-1}$.

while *b* values near 0.50 indicate that diffusion storage drives the electrochemical reaction. As shown in Fig. 4f, the peak current density is plotted against a sweep speed, and the *b* values obtained for oxidation (anodic) and reduction (cathodic) peaks are 0.5248 and 0.5278, respectively. As the *b* values of P–MCS-HSs are higher than 0.50, it can be concluded that P–MCS-HSs exhibited both surface- and diffusion-controlled redox reactions.

The GCD curves for the MCSHSs and MCOSs electrodes from 1 to 30 A $g^{-1}$ are shown in Figs. 5a, 5b. Figure 6a shows the GCD plots of P–MCS-HSs electrode measured in the voltage window (0.0 to +0.60) V vs. Ag/AgCl at various current densities (1, 3, 5, 10, 20, and 30 A $g^{-1}$). It can be seen from Fig. 6a that the electrode shows a highly symmetric GCD shape, implying impressive coulombic efficiency due to the reversible faradaic reactions during the charge-discharge cycle. All GCD plots also indicate a very small IR drop, which indicates excellent ionic transport, rate capability, and conductivity, due to their excellent coulombic efficiency. The estimated capacities of the P–MCS-HSs electrode are presented in comparison with those of the MCSHSs and MCOSs electrodes at different current densities (1, 3, 5, 10, 20, and 30 A $g^{-1}$), as indicated by the GCD plots. The P–MCS-HSs exhibited capacity values of 928.2, 901, 862.4, 806.3, 746.3, and 654.3 C $g^{-1}$ at 1, 3, 5, 10, 20, and 30 A $g^{-1}$, respectively, which were greater than MCSHSs and MCOSs electrodes. MCSHSs electrodes demonstrated capacities of 874, 850.25, 800, 700.25, 650, and 610.7 C $g^{-1}$ at 1, 3, 5, 10, 20, and 30 A $g^{-1}$, respectively. Accordingly, MCOSs exhibited 415, 395, 370, 345.25, 295, and 228.25 C $g^{-1}$ capacities at 1, 3, 5, 10, 20, and 30 A $g^{-1}$, respectively. As a result, the P–MCS-HSs electrode has a rate capability of 70.4%, which is significantly better than MCSHSs (69%) and MCOSs (55%) (Fig. 6b). To characterize super capacitive electrodes for actual applications, durability is important. In this way, as-prepared electrodes were tested up to 10000 charge/discharge cycles (at 10 A $g^{-1}$). In Fig. 6c, P–MCS-HSs electrode demonstrates 93.8% capacity retention and Coulombic efficiency reach about 92.2%, revealing excellent electrochemical reversibility and long-cycle durability.

The P–MCS-HSs electrode capacitance contributions are shown in Fig. 6D for sweep speeds ranging from 10 to 100 mV $s^{-1}$ the P–MCS-HSs electrode shows a diffusion-controlled contribution of 74.1% at 10 mV $s^{-1}$, declining to 13.4% at 100 mV $s^{-1}$. As a result, it can be concluded that the charge storage behavior of the P–MCS-HSs electrode is dependent on the diffusion-controlled transport process. It is expected that the P–MCS-HSs electrode shows excellent capacitive contributions and accelerates the electrode kinetics due to incorporating P in the porous network of the MCSHS electrode, resulting in enhanced charge storage.

It is evident from Fig. 7 that the P–MCS-HSs morphology retains its original structure after 10000 GCD cycles. Thus, P–MCS-HSs nanostructures are successfully prevented from degradation by graphene layers, resulting in superior longevity. All of the above features of supercapacitors can be summarized as follows: (1) P–MCS-HSs nanostructures provide both a large number of electroactive sites and facilitate the diffusion of the KOH electrolyte into the interior, thereby enhancing the electrolyte/electrode contact area for charge storage, (2) P elements introduced into the MCSHSs structure play a vital role in enhancing the conductivity as well as electrochemical stability of the materials, reactions and synergetic effect of the two components ensure their outstanding performance [95], (3) MCSHSs crystalline structure can be regulated by the incorporation of P atoms, providing more active sites for electrolytes to contact, and alleviating the strain on the P–MCS-HSs electrode during a long cycle, resulting in rapid electron transfer and improved structural stability. With all the above elec-

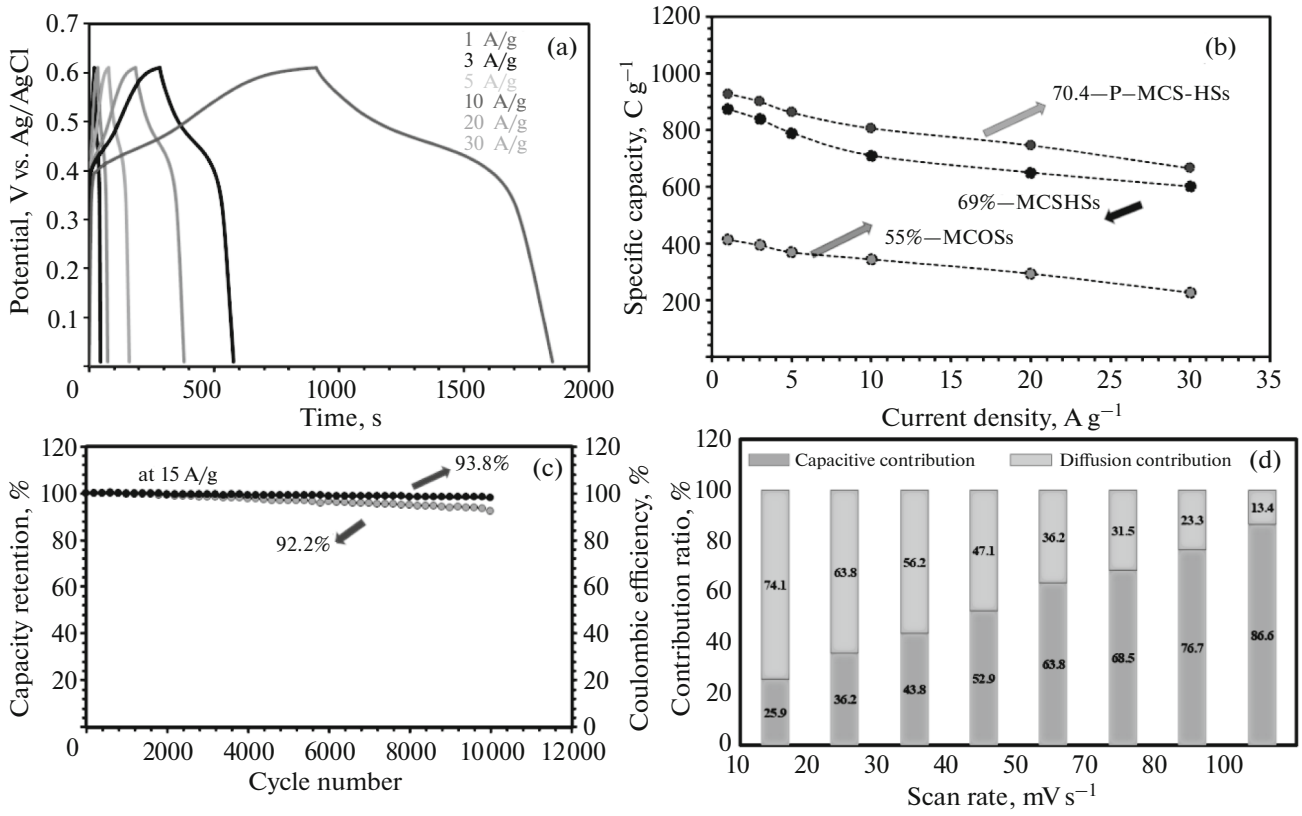


**Fig. 6.** (a) GCD curves of the MCSHSs at various current densities from 1 to 30 A/g. (b) GCD curves of the MCOSs at various current densities from 1 to 30 A/g.

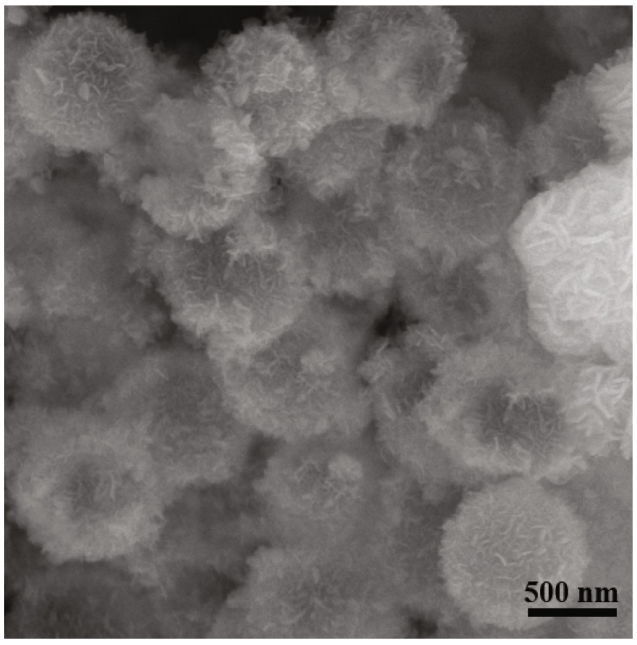


**Fig. 7.** FE-SEM images of the P–MCS-HSs after 10000 GCD cycles.

trochemical characteristics, the P–MCS-HSs electrode demonstrated outstanding super capacitive performance superior to formerly published transition metal sulfides and transition metal phosphides-based materials. According to Figs. 8a, 8b electrochemical tests were conducted on the AC electrode. According to the electrode, the capacitances at 1, 3, 5, 10, 20, and 30 A $g^{-1}$ were 185, 182.3, 178, 167.4, 152.3, and 137.2 F $g^{-1}$, respectively.

In order to verify that P–MCS-HSs is functional as the supercapacitor electrode in actual devices, P–MCS-HSs/NF cathode electrode, cellulose paper separator, and AC electrode anode electrode combinations were used to construct a hybrid supercapacitor device (denoted P–MCS-HSs /NF(+)‖AC/NF)(–))). It is crucial to determine an appropriate working voltage for P–MCS-HSs /NF(+)‖AC/NF)(–) apparatuses. Figure 9a presents the CV plots scanned at 60 mV $s^{-1}$ for both AC/NF and P–MCS-HSs/NF electrodes, illustrating that two electrodes run in the voltage windows of −1.0–0 and 0– to +0.60 V, respectively.

As a result, a cell voltage of 1.60 V is suitable for P–MCS-HSs/NF(+)‖AC/NF)(–) apparatuses. In

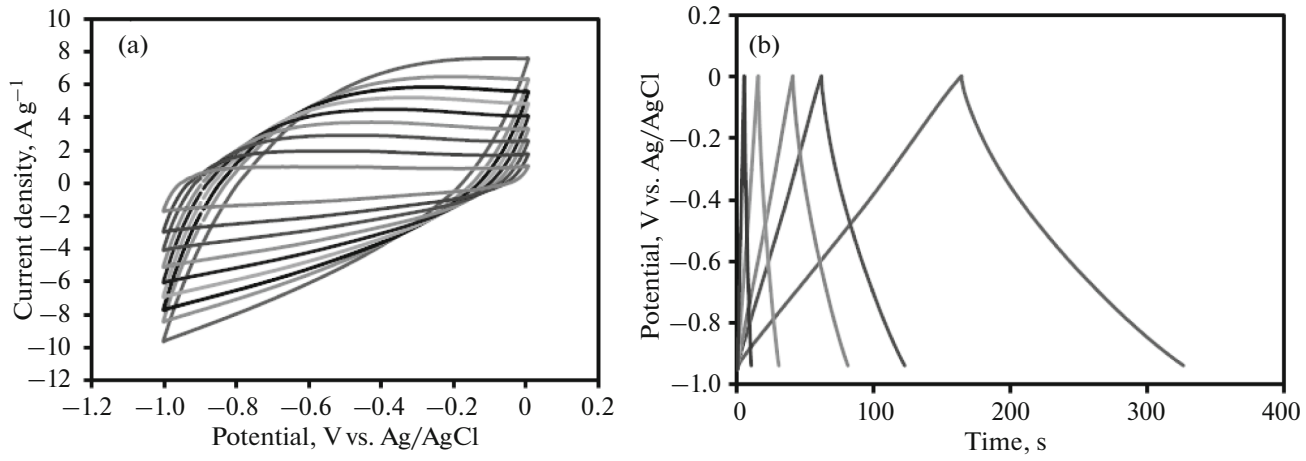


**Fig. 8.** (a) CV plots of the AC electrode from 10 to 100 mV/s. (b) GCD plots of the AC from 1 to 30 A/g.

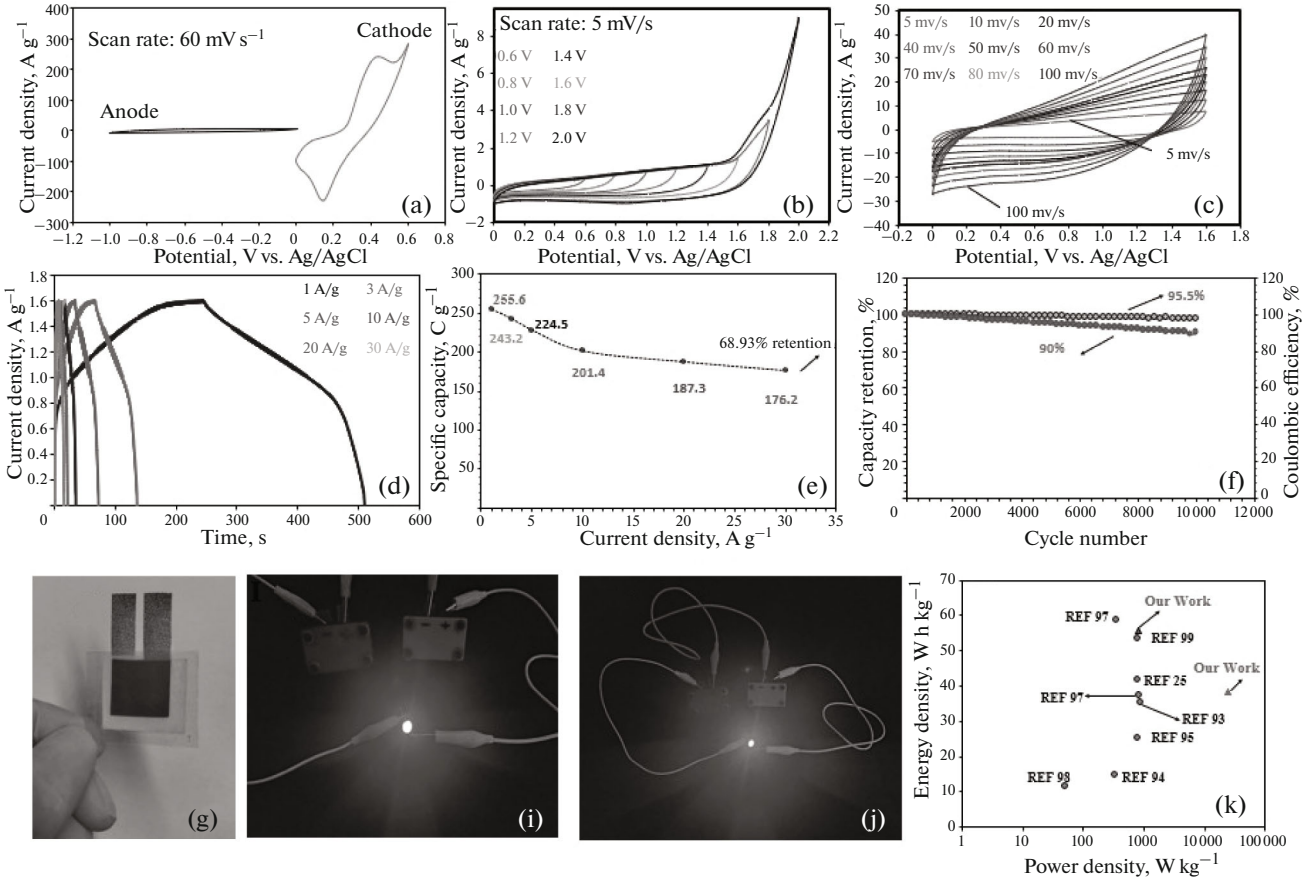


**Fig. 9.** (a) CV plots of AC/NF (anode electrode) and P–MCS-HSs/NF (cathode electrode) at 60 mV $s^{-1}$ in three-electrode cell. (b) CV plots of the P–MCS-HSs/NF(+)‖AC/NF)(–) at various potential window at 5 mV $s^{-1}$ from 0.6 to 2.0 V. (c) CV plots of the P–MCS-HSs/NF(+)‖AC/NF)(–) at various sweep rates from 5 to 100 mV $s^{-1}$. (d) GCD curves of the P–MCS-HSs/NF(+)‖AC/NF)(–) at different current densities from 1 to 30 A $g^{-1}$. (e) Variation of capacities of the P–MCS-HSs/NF(+)‖AC/NF)(–) as a function of current densities. (f) Longevity and Coulombic efficiency of the P–MCS-HSs/NF(+)‖AC/NF)(–) at 10 A $g^{-1}$. (i) Photograph image of the P–MCS-HSs/NF(+)‖AC/NF)(–). (i, j) Photographs of the red LED with two P–MCS-HSs/NF(+)‖AC/NF)(–) devices. (k) Comparison of the P–MCS-HSs/NF(+)‖AC/NF)(–) device's Ragone plot with various devices.

order to further confirm the stability of the P–MCS-HSs/NF(+)‖AC/NF)(–) apparatus, CV curves are measured under several voltage cells at 5 mV $s^{-1}$, as shown in Fig. 9b. According to Fig. 9b, when the voltage cell expanded to 1.6 V, polarization occurred on the related curve, reflecting that the suitable cell voltage of P–MCS-HSs/NF(+)‖AC/NF)(–) is 0–1.60 V. Based on these findings, 1.60 V is considered to be an appropriate voltage for conducting electrochemical measurements in cells.

Also, the effect of increasing sweep speed on CV shape is shown in Fig. 9c. All profiles have similar shapes, indicating satisfactory rate capability. Moreover, all CVs retained the reciprocal contributions from both faradic and non-faradic performances, as shown in the obtained profiles, which was confirmed by the faradic contribution of P–MCS-HSs/NF(+) and the capacitive contribution of AC/NF electrodes. The GCD plots of P–MCS-HSs/NF(+)‖AC/NF)(–) from 1 to 30 A $g^{-1}$ are shown in Fig. 9d. They possess relatively symmetrical characteristics, indicating reasonable coulombic efficiency and outstanding electrochemical reversibility behavior for this apparatus, which are reflected in Fig. 9d. It has been calculated that P–MCS-HSs /NF(+)‖AC/NF)(–) has specific capacities of 255.6, 243.2, 224.5, 201.4, 187.3, and 176.2 C $g^{-1}$ at 1, 3, 5, 10, 20, and 30 A $g^{-1}$, respectively, demonstrating 68.93% retention of capability (Fig. 9e). Our results indicate that our apparatus has a highly stabilized capacity retention capability. Hybrid supercapacitors must also be evaluated in order to determine their cyclic lifespan. As a result, the cyclic longevity of P–MCS-HSs/NF(+)‖AC/NF)(–) at 10 A $g^{-1}$ was evaluated with 10 000 uninterrupted GCD cycles (Fig. 9f). This P–MCS-HSs/NF(+)‖AC/NF)(–) demonstrates a capacity retention of 95.5% and a coulombic efficiency of 90%, demonstrating good cyclic longevity and electrochemical reversibility. Moreover, Fig. 9g illustrates the structure of the P–MCS-HSs/NF(+)‖AC/NF)(–) apparatus. The P–MCS-HSs/NF(+)‖AC/NF)(–) devices were connected in series to light up the red light-emitting diodes (LEDs) (Figs. 9i, 9j).

Figure 9k shows that the Ragone diagram illustrates the relationship between power and energy density. P–MCS-HSs/NF(+)‖AC/NF)(–) obtained a power density of 810.3 W $kg^{-1}$ at an energy density of 55.8 W h $kg^{-1}$. The apparatus also delivered a power density of 24453.6 W $kg^{-1}$ at 30 A $g^{-1}$ with an energy density of 38.26 W h $kg^{-1}$. Following Fig. 9k the proposed apparatus possesses higher energy densities than previously reported transition metal phosphide-based and transition metal sulfide-based supercapacitors [96–99].

## CONCLUSIONS

To summarize, MCOSs hollow spheres were successfully synthesized using a gas-liquid diffusion strategy. The morphology and surface characterization show a hollow sphere-like structure with several nanoporous sheets. A high-performance supercapacitor is attributed to the presence of two redox couple pairs and P doping. Moreover, P-doped material reduces strain during redox reactions and provides more reaction sites, thereby increasing pseudo capacitance and electrical activity. The Phosphorus-doped $MnCo_2S_4$ electrode material combines the benefits of transition metal sulfides with the merits of 3D porous network heterostructure, demonstrating substantial specific surface area and superior theoretical specific capacitance. Therefore, the specific capacity of this electrode can reach 928.2 C $g^{-1}$ at 1 A $g^{-1}$ and still preserve the initial specific capacitance of 93.8% after 10000 cycles. The assembled P–MCS-HSs/NF(+)‖AC/NF)(–) apparatus exhibits an ultra-high energy density of 55.8 W h $kg^{-1}$ at a power density of 810.3 W $kg^{-1}$. Additionally, it shows superb cyclic stability, with a durability rate of 95.5% after 10000 cycles. By using this method, a feasible synthesis method for preparing composite electrode materials for supercapacitors can be developed.

## FUNDING

This work was supported by ongoing institutional funding. No additional grants to carry out or direct thisparticular research were obtained.

## CONFLICT OF INTEREST

The authors of this work declare that they have no conflicts of interest.

## REFERENCES

1. H. Tabassum, A. Mahmood, B. Zhu, et al., Energy Environ. Sci. **12**, 2924 (2019). https://doi.org/10.1039/C9EE00315K
2. J. R. Miller and P. Simon, Science **321**, 651 (2008). https://doi.org/10.1126/science.1158736
3. B. Li, H. Cao, J. Shao, G. Li, et al., Inorg. Chem. **50**, 1628 (2011). https://doi.org/10.1021/ic1023086
4. B. Bayatsarmadi, Y. Zheng, A. Vasileff, et al., Small **13**, 1700191 (2017). https://doi.org/10.1002/smll.201700191
5. Y. Cheng, X. Xiao, K. Pan, et al., Chem. Eng. J. **380**, 122565 (2020). https://doi.org/10.1016/j.cej.2019.122565
6. B. Y. Guan, A. Kushima, L. Yu, et al., Adv. Mater. **29**, 1605902 (2017). https://doi.org/10.1002/adma.201605902
7. Z. Xu, J. Ren, Q. Meng, et al., ACS Sustain. Chem. Eng. **7**, 12447 (2019). https://doi.org/10.1021/acssuschemeng.9b02013

8. M. Amiri, S. E. Moosavifard, S. S. H. Davarani, S. K. Kaverlavani, et al., Chem. Eng. J. **420**, 129910 (2021). https://doi.org/10.1016/j.cej.2021.129910
9. M. Amiri, S. S. H. Davarani, S. K. Kaverlavani, et al., Appl. Surf. Sci. **527**, 146855 (2020). https://doi.org/10.1016/j.apsusc.2020.146855
10. A. Vlad, N. Singh, C. Galande, et al., Adv. Energy Mater. **5**, 201402115 (2015). https://doi.org/10.1002/aenm.201402115
11. J. Yan, Q. Wang, T. Wei, et al., Adv. Energy Mater. **4**, 201300816 (2014). https://doi.org/10.1002/aenm.201300816
12. Y. Zhang, C. Wang, H. Jiang, et al., Chem. Eng. J. **375**, 121938 (2019). https://doi.org/10.1016/j.cej.2019.121938
13. A. Muzaffar, M. B. Ahamed, K. Deshmukh, et al., Renewable Sustainable Energy Rev. **101**, 123 (2019). https://doi.org/10.1016/j.rser.2018.10.026
14. A. Afif, S. M. Rahman, A. T. Azad, et al., J. Energy Storage **25**, 100852 (2019). https://doi.org/10.1016/j.est.2019.100852
15. M. F. El-Kady, M. Ihns, M. Li, J. Y. Hwang, et al., Proc. Natl. Acad. Sci. **112**, 4233 (2015). https://doi.org/10.1073/pnas.1420398112
16. H. Hu, B. Y. Guan, and X. W. D. Lou, Chem. **1**, 102 (2016). https://doi.org/10.1016/j.chempr.2016.06.001
17. Y. Liu, N. Fu, G. Zhang, et al., Adv. Funct. Mater. **27**, 1605307 (2017). https://doi.org/10.1002/adfm.201605307
18. D. Wang, L. B. Kong, M. C. Liu, et al., Chem. Eur. J. **21**, 17897 (2015). https://doi.org/10.1002/chem.201502269
19. Q. Zong, H. Yang, Q. Wang, et al., Chem. Eng. J. **361**, 1 (2019). https://doi.org/10.1016/j.cej.2018.12.041
20. S. Liu, Y. Xu, C. Wang, et al., ChemElectroChem **6**, 5511 (2019). https://doi.org/10.1002/celc.201901504
21. P. Sun, C. Wang, W. He, et al., ACS Sustain. Chem. Eng. **5**, 10139 (2017). https://doi.org/10.1021/acssuschemeng.7b02143
22. D. Du, R. Lan, J. Humphreys, et al., J. Electrochem. Soc. **164**, A2881 (2017). https://doi.org/10.1149/2.0071713jes
23. Y. M. Chen, Z. Li, and X. W. Lou, Angew. Chem. **127**, 10667 (2015). https://doi.org/10.1002/ange.201504349
24. F. Mollaamin and M. Monajjemi, Russ. J. Phys. Chem. B **18**, 1199 (2024). https://doi.org/10.1134/S1990793124700519
25. F. Mollaamin and M. Monajjemi, Russ. J. Phys. Chem. B **18**, 1177 (2024). https://doi.org/10.1134/S1990793124700507
26. F. Mollaamin and M. Monajjemi, Russ. J. Phys. Chem. B **18**, 533 (2024). https://doi.org/10.1134/S199079312402012X
27. H. Li, Z. Li, Z. Wu, et al., J. Colloid Interface Sci. **549**, 105 (2019). https://doi.org/10.1016/j.jcis.2019.04.056
28. J. Cao, Y. Hu, Y. Zhu, et al., Chem. Eng. J. **405**, 126928 (2021). https://doi.org/10.1016/j.cej.2020.126928
29. J. Yu, X. Gao, Z. Cui, et al., Energy Technol. **7**, 1900018 (2019). https://doi.org/10.1002/ente.201900018
30. F. Mollaamin, S. Shahriari, and M. Monajjemi, Russ. J. Phys. Chem. B **18**, 398 (2024). https://doi.org/10.1134/S199079312402026X
31. X. Wang, J. Hu, W. Liu, et al., J. Mater. Chem. A **3**, 23333 (2015). https://doi.org/10.1039/C5TA07169K
32. C. Cheng, D. Kong, C. Wei, et al., Dalton Trans. **46**, 5406 (2017). https://doi.org/10.1039/C7DT00355B
33. W. Wei, L. Mi, Y. Gao, et al., Chem. Mater. **26**, 3418 (2014). https://doi.org/10.1021/cm5006482
34. B. S. Soram, I. S. Thangjam, J. Y. Dai, et al., Chem. Eng. J. **395**, 125019 (2020). https://doi.org/10.1016/j.cej.2020.125019
35. Q. Liu, X. Hong, X. You, et al., Energy Storage Mater. **24**, 541 (2020). https://doi.org/10.1016/j.ensm.2019.07.001
36. C. Yu, Y. Li, Y. Wang, et al., ACS Sustainable Chem. Eng. **8**, 11491 (2020). https://doi.org/10.1021/acssuschemeng.0c00716
37. Y. Gao and L. Zhao, Chem. Eng. J. **430**, 132745 (2022). https://doi.org/10.1016/j.cej.2021.132745
38. H. Sabeeh, S. Zulfiqar, M. Aadil, et al., Ceram. Int. **46**, 21064 (2020). https://doi.org/10.1016/j.ceramint.2020.05.179
39. X. Yu, J. Yu, L. Hou, et al., J. Power Sources **408**, 65 (2018). https://doi.org/10.1016/j.jpowsour.2018.10.082
40. K. Zhang, Y. Xu, Y. Lin, et al., Chin. Chem. Lett. **32**, 3553 (2021). https://doi.org/10.1016/j.cclet.2021.02.034
41. Z. Lu, Y. Zhang, M. Sun, P. Zou, et al., J. Power Sources **516**, 230685 (2021). https://doi.org/10.1016/j.jpowsour.2021.230685
42. S. Li, Y. Yang, Z. Hu, et al., Electrochim. Acta **424**, 140604 (2022). https://doi.org/10.1016/j.electacta.2022.140604
43. F. Mollaamin and M. Monajjemi, Russ. J. Phys. Chem. B **18**, 49 (2024). https://doi.org/10.1134/S1990793124010159
44. F. Mollaamin and M. Monajjemi, Russ. J. Phys. Chem. B **18**, 607 (2024). https://doi.org/10.1134/S1990793124020271
45. F. Mollaamin, Russ. J. Phys. Chem. B **18**, 805 (2024). https://doi.org/10.1134/S1990793124700131
46. D. Guo, Y. Zhang, W. Sun, et al., ACS Appl. Mater. Interfaces **11**, 41580 (2019). https://doi.org/10.1021/acsami.9b11894
47. J. Zhang, T. Yan, J. Fang, et al., Environ. Sci. Nano **7**, 926 (2020). https://doi.org/10.1039/C9EN01216H

48. E. Baasanjav, P. Bandyopadhyay, G. Saeed, et al., J. Ind. Eng. Chem. **99**, 299 (2021). https://doi.org/10.1016/j.jiec.2021.04.034
49. X. Tan, Z. Feng, W. Yang, et al., ACS Appl. Energy Mater. **6**, 702 (2023). https://doi.org/10.1021/acsaem.2c02837
50. Y. Yang, H. Zhu, H. Meng, et al., J. Mater. Sci. **56**, 3280 (2021). https://doi.org/10.1007/s10853-020-05407-7
51. M. Zhang, H. Du, Z. Wei, et al., ACS Appl. Energy Mater. **4**, 8262 (2021). https://doi.org/10.1021/acsaem.1c01507
52. Y. Wen, Y. Liu, T. Wang, et al., ACS Appl. Energy Mater. **4**, 6531 (2021). https://doi.org/10.1021/acsaem.1c00557
53. J. Xu, C. Xiang, S. Fang, et al., J. Energy Storage **44**, 103267 (2021). https://doi.org/10.1016/j.est.2021.103267
54. R. Mohammadi, L. Naderi, and S. Shahrokhian, J. Alloys Compd. **811**, 152016 (2019). https://doi.org/10.1016/j.jallcom.2019.152016
55. A. M. Elshahawy, X. Li, H. Zhang, et al., J. Mater. Chem. A **5**, 7494 (2017). https://doi.org/10.1039/C7TA00943G
56. T. T. Nguyen, J. Balamurugan, V. Aravindan, et al., Chem. Mater. **31**, 4490 (2019). https://doi.org/10.1021/acs.chemmater.9b01101
57. I. Chakraborty, K. J. Bodurtha, N. J. Heeder, et al., ACS Appl. Mater. Interfaces **6**, 16472 (2014). https://doi.org/10.1021/am5044592
58. J.-G. Wang, D. Jin, R. Zhou, et al., ACS Nano 10, 6227 (2016). https://doi.org/10.1021/acsnano.6b02319
59. A. Bahaa, J. Balamurugan, N. H. Kim, et al., J. Mater. Chem. A **7**, 8620 (2019). https://doi.org/10.1039/C9TA00265K
60. Y. Zhang, X. Jing, Y. Cheng, et al., Inorg. Chem. Front. **5**, 2798 (2018). https://doi.org/10.1039/C8QI00728D
61. X. Wang, J. Feng, Y. Bai, et al., Rev. **116**, 10983 (2016). https://doi.org/10.1021/acs.chemrev.5b00731
62. L. Ji, Y. Zhu, X. Teng, et al., Sci. Bull. **67**, 398 (2022). https://doi.org/10.1016/j.scib.2021.10.008
63. L. Shen, L. Yu, X. Y. et al., Angew. Chem. Int. Ed. **54**, 1868 (2015). https://doi.org/10.1002/anie.201409776
64. Y. Guo, C. Wu, N.-W. Li, et al., J. Mater. Chem. A **7**, 25247 (2019). https://doi.org/10.1039/C9TA05790K
65. X. Yin, H. Li, H. Wang, et al., ACS Appl. Mater. Interfaces 10, 29496 (2018). https://doi.org/10.1021/acsami.8b08455
66. S. Yadav and A. Sharma, J. Energy Storage **44**, 103295 (2021). https://doi.org/10.1016/j.est.2021.103295
67. C. Guan, X. Liu, W. Ren, et al., Adv. Energy Mater. **7**, 1602391 (2017). https://doi.org/10.1002/aenm.201602391
68. N. Zhou, J. Zu, F. Xu, et al., J. Mater. Sci.: Mater. Electron. **31**, 12961 (2020). https://doi.org/10.1007/s10854-020-03849-y
69. S. Liu, Y. Yin, Y. Shen, et al., Small **16**, 1906458 (2020). https://doi.org/10.1002/smll.201906458
70. W. Chu, Z. Shi, Y. Hou, et al., ACS Appl. Mater. Interfaces **12**, 2763 (2019). https://doi.org/10.1021/acsami.9b13182
71. W. Liu, E. Hu, H. Jiang, et al., Nat. Commun. **7**, 10771 (2016). https://doi.org/10.1038/ncomms10771
72. C. Lu, Y. Gao, W. An, et al., Colloids Surf. A Physicochem. Eng. Asp. **659**, 1 30783 (2023). https://doi.org/10.1016/j.colsurfa.2022.130783
73. L. Wan, Y. Wang, Y. Zhang, et al., J. Chem. Eng. **415**, 128995 (2021). https://doi.org/10.1016/j.cej.2021.128995
74. S. Kamari Kaverlavani, L. Abbasi, Y. K. Mishra, et al., ACS Sustainable Chem. Eng. **10**, 13310 (2022). https://doi.org/10.1021/acssuschemeng.2c02513
75. A. Laheäär, P. Przygocki, Q. Abbas, et al., Electrochem. Commun. **60**, 21 (2015). https://doi.org/10.1016/j.elecom.2015.07.022
76. K. V. G. Raghavendra, C. V. M. Gopi, R. Vinodh, et al., J. Energy Storage **27**, 101159 (2020). https://doi.org/10.1016/j.est.2019.101159
77. H. Wang, K. Zhang, Y. Song, et al., Carbon **146**, 420 (2019). https://doi.org/10.1016/j.carbon.2019.02.035
78. T. I. Singh, G. Rajeshkhanna, T. Kshetri, et al., J. Mater. Chem. A **8**, 26158 (2020). https://doi.org/10.1039/D0TA06348G
79. Y. Guo, J. Tang, H. Qian, et al., Chem. Mater. **29**, 5566 (2017). https://doi.org/10.1021/acs.chemmater.7b00867
80. Y. V. Kaneti, Y. Guo, N. L. W. Septiani, et al., J. Chem. Eng. **405**, 126580 (2021). https://doi.org/10.1016/j.cej.2020.126580
81. Y. Ma, Y. Ma, G. T. Kim, T. Diemant, et al., Adv. Energy Mater. **9**, 201902077 (2019). https://doi.org/10.1002/aenm.201902077
82. W. Liu, H. Gao, Z. Zhang, et al., J. Chem. Eng. **437**, 135352 (2022). https://doi.org/10.1016/j.cej.2022.135352
83. C. Wang, G. Sui, D. Guo, et al., J. Colloid Interface Sci. **599**, 577 (2021). https://doi.org/10.1016/j.jcis.2021.04.118
84. W. Jiang, F. Hu, Q. Yan, et al., Inorg. Chem. Front. **4**, 1642 (2017). https://doi.org/10.1039/C7QI00391A
85. R. Gilliam, J. Graydon, D. Kirk, et al., Int. J. Hydrogen Energy **32**, 359 (2007). https://doi.org/10.1016/j.ijhydene.2006.10.062
86. P. Li, S. Liu, Y. Mao, et al., ACS Appl. Energy Mater. **4**, 9178 (2021). https://doi.org/10.1021/acsaem.1c01316
87. L. Lyu, W. H. Antink, B.-H. Lee, et al., ACS Appl. Energy Mater. **4**, 10553 (2021). https://doi.org/10.1021/acsaem.1c01493
88. H. M. El Sharkawy, D. M. Sayed, A. S. Dhmees, et al., ACS Appl. Energy Mater. **3**, 9305 (2020). https://doi.org/10.1021/acsaem.0c01630

89. Y. Yang, Q. Ma, L. Han, et al., Inorg. Chem. Front. **6**, 1398 (2019). https://doi.org/10.1039/C9QI00273A
90. Y. Al Haj, J. Balamurugan, N. H. Kim, et al., J. Mater. Chem. A **7**, 3941 (2019). https://doi.org/10.1039/C8TA12396A
91. Y. Wen, B. Wang, C. Huang, et al., Chem. Eur. J. **21**, 80 (2015). https://doi.org/10.1002/chem.201404779
92. X. Feng, Y. Bai, M. Liu, et al., J. Energy. Environ. Sci. **14**, 2036 (2021) https://doi.org/10.1039/D1EE00166C
93. L. Zhi, W. Zhang, L. Dang, et al., J. Power Sources **387**, 108 (2018). https://doi.org/10.1016/j.jpowsour.2018.03.063
94. A. M. Zardkhoshoui and S. S. H. Davarani, Sustain. Energy Fuels **5**, 900 (2021). https://doi.org/10.1039/D0SE01665A
95. M. Xie, M. Zhou, Y. Zhang, et al., J. Colloid Interface Sci. **608**, 79 (2022). https://doi.org/10.1016/j.jcis.2021.09.159
96. H. C. Chen, S. Jiang, B. Xu, et al., J. Mater. Chem. A **7**, 6241 (2019). https://doi.org/10.1039/C8TA11189H
97. Y. Dong, X. Yue, Y. Liu, et al., J. Colloid Interface Sci. **628**, 222 (2022). https://doi.org/10.1016/j.jcis.2022.08.033
98. S. He, Z. Li, H. Mi, et al., J. Power. Sources **467**, 228324 (2020). https://doi.org/10.1016/j.jpowsour.2020.228324
99. F. Wang, H. Lei, H. Peng, et al., Electrochim. Acta. **325**, 134934 (2019). https://doi.org/10.1016/j.electacta.2019.134934
100. M. Gao, W.-K. Wang, X. Zhang, et al., J. Phys. Chem. C **122**, 25174 (2018). https://doi.org/10.1021/acs.jpcc.8b07716
101. M. Zhang, H. Du, Z. Wei, et al., ACS Appl. Energy Mater. **5**, 186 (2021). https://doi.org/10.1021/acsaem.1c02730
102. Y. Xu, S. Xiong, S. Weng, et al., New J. Chem. **44**, 6810 (2020). https://doi.org/10.1039/D0NJ00531B
103. X. Zhang, J. Wang, Y. Sui, et al., ACS Appl. Nano Mater. **3**, 11945 (2020). https://doi.org/10.1021/acsanm.0c02507
104. L. Wan, Y. Yuan, J. Liu, et al., Electrochim. Acta **368**, 137579 (2021). https://doi.org/10.1016/j.electacta.2020.137579
105. R. Liu, J. Huang, Y. Diao, et al., J. Colloid Interface Sci. **639**, 263 (2023). https://doi.org/10.1016/j.jcis.2023.02.074
106. Z. Ji, K. Liu, L. Chen, Y. Nie, D. Pasang, Q. Yu, et al., J. Colloid Interface Sci. **609**, 503 (2022). https://doi.org/10.1016/j.jcis.2021.11.055